

This work has been submitted to the IEEE for possible publication. Copyright may be transferred without notice, after which this version may no longer be accessible.

Localized Motion Artifact Reduction on Brain MRI Using Deep Learning with Effective Data Augmentation Techniques

Yijun Zhao*, Jacek Ossowski†, Xuming Wang*, Shangjin Li*, Orrin Devinsky‡, Samantha P. Martin‡, Heath R. Pardoe‡

* Computer and Information Science Department, Fordham University, New York, NY, USA

†QS Investors, LLC, New York, NY 10022 USA

‡NYU Langone School of Medicine, New York, NY 10013 USA

Abstract—In-scanner motion degrades the quality of magnetic resonance imaging (MRI) thereby reducing its utility in the detection of clinically relevant abnormalities. We introduce a deep learning-based MRI artifact reduction model (DMAR) to localize and correct head motion artifacts in brain MRI scans. Our approach integrates the latest advances in object detection and noise reduction in Computer Vision. Specifically, DMAR employs a two-stage approach: in the first, degraded regions are detected using the Single Shot Multibox Detector (SSD), and in the second, the artifacts within the found regions are reduced using a convolutional autoencoder (CAE). We further introduce a set of novel data augmentation techniques to address the high dimensionality of MRI images and the scarcity of available data. As a result, our model was trained on a large synthetic dataset of 217,000 images generated from six whole brain T1-weighted MRI scans obtained from three subjects. DMAR produces convincing visual results when applied to both synthetic test images and 55 real-world motion-affected slices from 18 subjects from the multi-center Autism Brain Imaging Data Exchange study. Quantitatively, depending on the level of degradation, our model achieves a 14.3%–25.6% reduction in RMSE and a 1.38–2.68 dB gain in PSNR on a 5000-sample set of synthetic images. For real-world scans where the ground-truth is unavailable, our model produces a 3.65% reduction in regional standard deviations of image intensity.

Index Terms—MRI, motion artifact reduction, machine learning, object detection, k-space

I. INTRODUCTION

MRI acquisition often requires extended amounts of time within which patients are asked to remain motionless. Even with full cooperation subject movement is inevitable resulting in deleterious image artifacts. We propose a deep learning-based MRI artifact reduction model (DMAR) for retrospective correction of motion artifacts in brain MRI scans. Our model targets the typical ringing artifacts caused by in-scanner head motion during the MRI acquisition. Because these rings appear in various sections of the images, we design our DMAR model in two stages. In the first stage, we employ the Single Shot Multibox Detector (SSD [1]) to localize the regions with ringing artifacts. In the second, we train a convolutional autoencoder (CAE, [2]) to reduce the artifacts in the regions identified by the localizer. There are two primary challenges

associated with our approach: 1) motion-related artifacts cause errors in the initial time-domain signals, which manifest as spatially extended distortions, and 2) the high dimensionality of imaging datasets versus the relatively limited amount of training data. We address the first challenge by modeling the ringing artifacts as controlled perturbations in the k -space representation of an MRI scan [3]–[5] as well as by modulating the original scan’s pixel intensities. The second challenge is addressed by augmentation of a limited number of motion-free MRI scans; we obtain a large number of synthetic motion-free images by applying smooth transformations that alter proportions of the subjects’ morphological features. As a result, we have generated a set of 217,000 artificial images facilitating the training of our deep-learning model. We present the details of the image generation process in Section III-B.

We evaluate our model’s performance using both a synthetic dataset of 5000 artificially corrupted images with various degradation levels and a set of motion-affected scans from the multi-center Autism Brain Imaging Data Exchange (ABIDE) study [6]. We use three quantitative measures: the pixel-wise root mean squared error (RMSE) and peak signal to noise ratio (PSNR) [7] applied to our synthetic image dataset, and regional standard deviations of image intensities assessed in real-world images where the ground truth is unavailable. Details are provided in Section IV.

The main contribution of our study is the two-stage approach to reduce motion artifacts in MRI brain scans. Existing methodologies typically apply a correction model to the entire image. Our experiments indicate that this nonselective approach can overcompensate in regions where the artifacts are less prominent. Moreover, the two models we developed in each stage are independent; they can be integrated (as in our DMAR model) or applied to separate tasks where each could be of value. Our work also introduces a set of new augmentation techniques to generate large numbers of realistic MRI images (both motion-free and motion-affected). DMAR was effectively trained on synthetic data, demonstrating the feasibility of our approach and its potential to significantly advance the application of deep learning to medical image

analysis.

II. RELATED WORK

In the area of artifact localization Lorch et al. [8] studied detection of motion-affected regions using a supervised learning approach based on random decision forests. Both the effects of respiratory motion on cardiac scans and of bulk patient motion in the acquisition of head scans were studied. Kustner et al. [9] provided a method for spatially resolved detection of motion artifacts in MR images of the head and abdomen. In their study, images were divided into partially overlapping patches of different sizes achieving spatial separation. Using these patches as input data, a convolutional neural network (CNN) was trained to derive probability maps for the presence of motion artifacts in the patches. The authors concluded that identifying motion artifacts in MRI is feasible with good accuracy in the head and abdomen.

We are the first to apply the latest deep object detection model (i.e., SSD) to localize motion artifacts in brain MRI scans. Our experimental results demonstrate the great practical utility of the approach as evidenced by the model's high mAP score (Section III-D1).

On the subject of retrospective correction of image noise, Zhang et al. [10] introduced a deep convolutional network which reduced image artifacts resulting from Gaussian noise with unknown noise level and showed a way to apply their network to other reconstruction problems such as single image super resolution and JPEG image deblocking.

In more recent work, Lyu et al. [11] proposed an approach to improving the quality of MR images using the ensemble of five generative adversarial networks (GANs) each working with a data set produced by a different conventional image super resolution method. They found that the ensemble outperformed any single sub-network and produced results superior to those of other deep learning-based super-resolution methods.

Pawar et al. [12] apply deep learning methods to the problem of reconstruction of artifact-free MRI scans from their randomly undersampled k -spaces. They transform the problem to that of pixel classification, and solve it using a deep learning classification network. While we also operate in the k -space domain, our methods are different. Moreover, their work focuses on general artifacts that tend to affect the entire image, while ours concentrates on ringing artifacts that only occur in localized regions of a scan.

III. MATERIAL AND METHODS

We utilized a two-stage process for correcting motion-related ringing artifacts in structural MRI scans (Figure 1). All analyses were carried out on individual MRI slices. Ringing artifacts were first localized in an image using the Single Shot Multibox Detector (SSD), and the identified regions were then corrected using a denoising convolutional autoencoder (CAE). The CAE model was trained by following the supervised learning paradigm in which a set of corrupted images is provided and the network learns to reconstruct the corresponding artifact-free images which are provided as

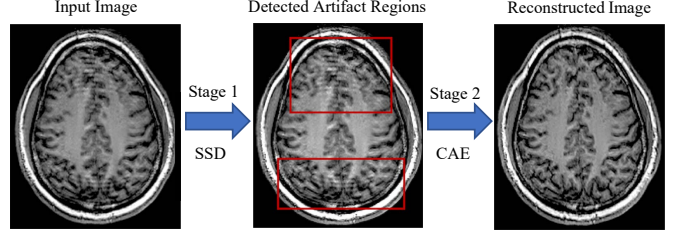


Fig. 1: Two-stage Approach to Reduction of Motion Artifacts. SSD: Single Shot MultiBox Detector. CAE: Convolutional Autoencoder.

the ground truth. Since both models require large amount of training data, augmentation techniques were used to generate a large set of artifact-free slices and their corresponding artifact-corrupted counterparts.

A. Data Acquisition

1) *Model Training*: The large synthetic image dataset was generated from six whole brain T1-weighted MRI scans of three healthy adults. Participants were imaged on a 3T Siemens Prisma MRI scanner with the following acquisition parameters: Whole-brain T1-weighted 3D MPRAGE, 1mm isotropic voxel size, Echo time (TE) = 2.99 ms, Inversion time (TI) = 900 ms, Repetition time (TR) = 2.5 s, flip angle = 8 degrees. Participants were instructed to hold their heads still. Sagittal slices from these acquisitions were then used to generate synthetic motion-free images as well as their corrupted versions with localized image artifacts (Section III-B). A total of 217,000 of such pairs were generated to facilitate training of our artifact localization and reduction models.

2) *Model Testing*: The model was tested on both synthetic and real-world MRI slices. A synthetic test set with 5000 image pairs was generated from a motion-free scan of a new subject following the same process as in the model training. To study our model's performance at various levels of corruption, we made it contain 1000 images in each of the following degradation intervals as indicated by PSNR: <17, [17, 18), [18, 19), [19, 20), and [20, 21). The set was used for quantitative evaluation of our model's performance using PSNR and RMSE measures.

The model was further applied to 18 T1-weighted MRI scans selected from the ABIDE study [6]. These scans were selected from a larger dataset that had been visually evaluated as low quality in a previous study [13]. Image slices from the three cardinal planes (axial, coronal and sagittal) were used to validate our model as measured by the standard deviations of image intensity within motion-affected regions identified using the SSD (Section IV-C).

Qualitative visual assessment was performed on both test datasets.

B. Data Augmentation

Three augmentation methods were used to generate our training data for both stages of the DMAR model. To learn

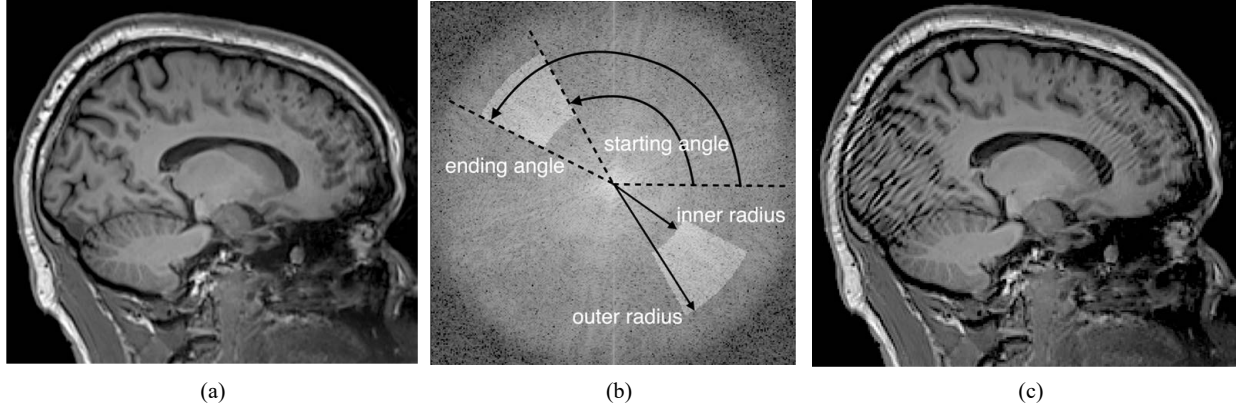


Fig. 2: *k*-space Based Artifact Generation. (a) Original image; (b) Symmetric, centered annular sector is modified in the *k*-space of the image; the sectors' elements are uniformly scaled and their phase is shifted by the same angle; inverse FT is applied to obtain an artifact image (not shown) (c) Synthetic image with “ringing” artifacts obtained by superimposing the original image with a random collection of circular regions from the artifact image constructed in (b).

detecting the artifacts, the localizer required a set C of artifact-free images, a set D of the degraded versions of images in C , and a set B of collections of bounding boxes locating the artifacts in D . The autoencoder model used the same sets C and D to learn the reconstruction function which produced the best approximation of a motion-free image from a corrupted one. To accommodate these needs, our methods produce i) a large dataset of realistic motion-free images based on a limited number of real-world scans (Section III-B1), and ii) a corresponding set of corrupted images with localized ringing artifacts (Sections III-B2 and III-B3). These synthetic artifacts were modeled on real-world motion-affected MRI scans from the ABIDE database. The ABIDE images were visually inspected to determine the types of degradations that are likely to occur in real-world imaging datasets. Based on these images, we simulated the “ringing” and “rippling” artifacts which we combined in the 2:1 proportion in our final dataset.

1) *Modeling inter-subject brain morphological variability:* We applied local spatial distortions to simulate natural inter-subject variability in brain morphology. These deformations were performed in a varying set of three to eight non-overlapping circles within each motion-free image. The number and location of the circles changed randomly from image to image and their radii were chosen to be maximal while still allowing no overlaps (resulting in frequent tangent pairs). Within each circle, a radial stretching was applied with a smoothly changing ratio that equaled 1.0 both at the circle’s center and its border. This ensured that the created deformations were localized, had no discontinuities, and blended smoothly with the unaffected areas. The stretching ratio varied according to the formula:

$$\text{IMG}_{\text{new}}(P) = \text{IMG}_{\text{old}}(C + u^{(1+\epsilon)}(P - C))$$

where $\text{IMG}_{\text{new}}(P)$ is the new pixel intensity at a given point P in a circle with the center C and radius R , and $u = \text{distance}(P, C)/R$. We have found that setting $\epsilon=0.2$ resulted in a moderate amount of deformation and provided great variability between the images. The obtained transformations are quite subtle in that an untrained observer may not notice them unless the images are viewed in quick succession (e.g., in an [animation](#)). This process allowed us to generate hundreds of different images from a single MRI slice and ultimately to create a large data set of 217,000 images using a limited number of high quality MRI scans.

2) *k*-space based synthetic artifact generation: Raw MRI data is encoded in *k*-space, representing the spatial frequencies of the object being imaged. The *k*-space data is then converted into the human-recognizable MRI scan by the application of an inverse Fourier transform (FT). In-scanner head motion during the scan introduces errors as *k*-space is filled that manifest as ringing, ghosting or blurring artifacts following the inverse FT. Therefore artifacts similar to those encountered in clinical imaging can be generated by modifying the FT of a motion-free image in *k*-space and applying an inverse FT. We modified the *k*-space data of a given image by selecting a symmetric, centered annular sector and applied a uniform phase shift and scaling of the magnitude of the annular sector’s elements (Figure 2).

We utilized three sets of base parameters (Table 1) to create synthetic artifacts that resembled real-world artifacts in images from the ABIDE study. In each of the base sets three subgroups of the parameters, a) inner and outer radii, b) modulus magnification, c) starting and ending angles of the annular sectors, were randomly shifted by multiples of 2-3 pixels, 0.2, and 11° - 29° respectively. This resulted in the annular areas’ uniformly covering the whole mid-to-high frequency section of the Fourier spectrum as they varied from image to image.

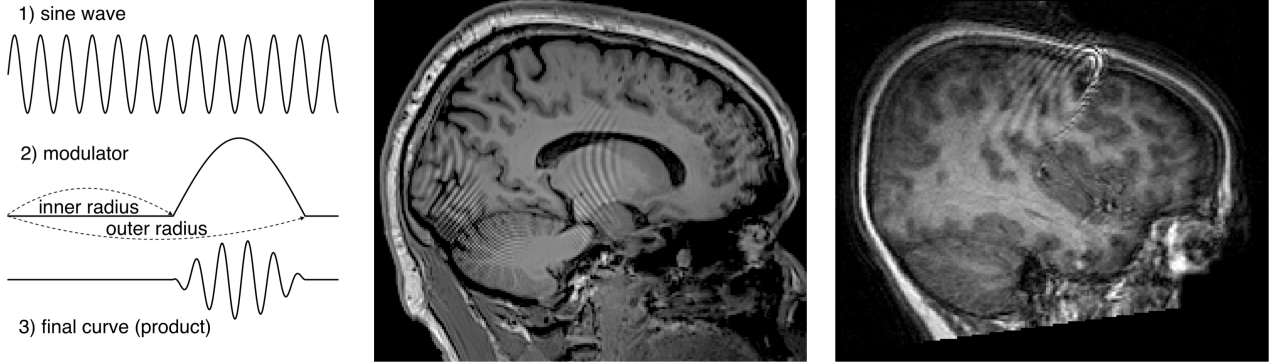


Fig. 3: Synthetic Elliptic Artifact Generation. (a) Three-step process for generating elliptic intensity variations. S is a sine wave that propagates elliptically from a randomly chosen center in a given image. M is a modulator curve consisting of the positive part of the sine function extended between random inner and outer radii. Pixel intensities in the image are multiplied by $1 + M * S$; (b) sample synthetic artifact; (c) sample real-world elliptic artifact.

TABLE I: Sample Base Combination of Annular Parameters

Parameter	Comb. 1	Comb. 2	Comb. 3
inner radius (pixels)	61	55	60
outer radius (pixels)	66	105	80
phase shift	144°	29°	9°
modulus magnification	9	8	6
annular sector starting angle	10°	29°	11°
annular sector ending angle	38°	57°	46°

Following these k -space operations we applied an inverse FT to convert to image space and obtain an artifact image that suffered degradation across its whole area. To localize the corruption, we copied a random collection of circular ROIs with random sizes and locations from the artifact image onto the original clear scan to obtain a set of localized artifacts. The final distorted image was intensity histogram matched with the original image to prevent pixel intensity shifts. We thereby generated in this fashion hundreds of motion-affected images from a single high quality slice. In addition, our random number generator settings ensured that the centers, radii, angles, frequencies, and magnitudes we employed in sizing and positioning of the artifacts were different on every synthetic image.

3) '*Rippling*' artifacts generation: Some MRI scans contain artifacts that appear as spatially localized elliptic artifacts that resemble a rippling effect (Figure 3). We supplemented the approach described in III-B2 by applying elliptic intensity modulations on motion-free slices. The effect was obtained by following a three-step process (Figure 3 (a)): 1) generating a sine wave S that propagated elliptically from a randomly chosen center point, 2) generating a modulator curve M which consisted of the positive part of the sine function extended between random inner and outer radii, and 3) multiplying the scan's pixel intensities by $1 + M * S$. The frequency of the initial wave and the amplitude of the modulator were chosen

randomly giving rise to hundreds of artifacts per original image. As described in Section III-B2, to further localize the degradation, a random set of circular ROIs was extracted from the artifact image and superimposed over the clear scan (Figure 3(b)). We present an example of real-world scan manifesting such artifacts in Figure 3(c).

C. Deep MRI Artifact Reduction (DMAR) Model

Figure 4 presents the two-step pipeline of our DMAR model. To implement the localization component (upper diagram), we investigated different state-of-the-art models including the Single Shot MultiBox Detector (SSD) [1] and Mask R-CNN [14], and selected SSD for its better accuracy and computational efficiency. We briefly describe the SSD model and our customizations in Section III-C1. In the second step (bottom part of the diagram), DMAR applies a convolutional autoencoder (CAE) to reduce the artifacts within the regions identified by the localizer. The CAE network and our customizations are introduced in Section III-C2.

1) *Single Shot MultiBox Detector (SSD)* : Unlike other object detection systems [14]–[16] where the object localization (i.e., bounding box positions) and classification are carried out by two separate networks, SSD [1] accomplishes both tasks in a single network, which is computationally more efficient and easier to integrate into systems that require a detection sub-system. The SSD internal architecture consists of a base convolutional neural network (CNN) for extracting relevant image features and additional feature layers to allow for object detection at differing spatial scales. We experimented with two established CNN networks that are often applied in their entirety or as components to computer vision problems: the VGG [17] and ResNet [18], ultimately settling on VGG-16.

The SSD outputs (i) bounding boxes indicating the location of detected artifacts, and (ii) a score between 0 and 1 indicating the likelihood that each bounding box corresponds to an object of the specified type. For our study, we trained the SSD to

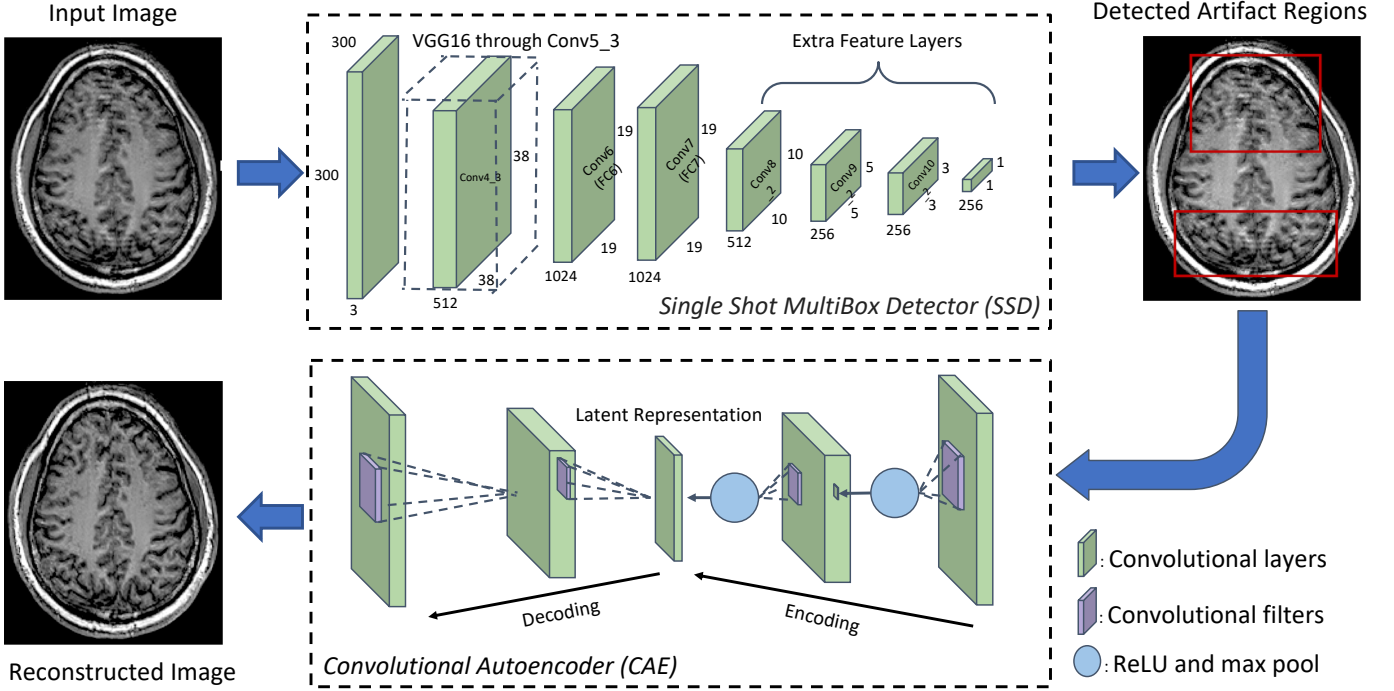


Fig. 4: DMAR Model Architecture. SSD outputs detected regions with artifacts as indicated by the red boxes. CAE reconstructs the image within the boxed regions.

detect a single object type, i.e., an artifact, with multiple occurrences possible per slice. We trained our SSD model using the synthetic datasets described in Section III-A with a 9:1 split for training and validation. The input to the model were the images superimposed with localized artifacts. The ground-truth bounding boxes were the circumscribing squares of all ROIs generated during the data augmentation process. The evaluation of our SSD implementation is presented in Section IV-A.

2) *Convolutional Autoencoder (CAE)* : A CAE is a deep learning approach that combines the power of a convolutional neural network (CNN, [19]) and an autoencoder [2]. The former extracts defining features from images and the latter has been widely applied to data compression and image noise reduction. Integration of the two approaches has delivered promising results in tasks such as object recognition [18], [20], image captioning [21], [22] and image restoration [23], [24].

Our model is inspired by a variant of an autoencoder, the *denoising* autoencoder ([25], [26]), which takes as input a set of degraded images and is forced to output the corresponding artifact-free images. In the training, both the MRI images corrupted with motion artifacts as well as their clear versions are provided following the standard supervised learning scheme.

There are five hidden layers in our network. The size, stride, and number of filters for each layer are presented in Table II. We train the model using the synthetic dataset with 217,000 pairs of images (Section III-A). Of these, 163,125 pairs were

TABLE II: Architecture of Our CAE Model

	Filter Size	Stride	# of Filters
Convolutional Layer1	4x4	(1,1)	64
Convolutional Layer2	16x16	(1,1)	128
Convolutional Layer3	1x1	(1,1)	256
Transpose Conv. Layer 1	8x8	(1,1)	32
Transpose Conv. Layer 2	1x1	(1,1)	1

used for training and 52,200 for validation. Slices that did not contain any brain tissue were excluded from our analysis. The evaluation of the CAE component is presented in Sections IV-B and IV-C.

D. Quantitative Efficacy Measures

1) *Localization Model*: To perform well an object detector needs to excel in 1) determining the location of objects (i.e., a regression task), and 2) deciding the type of located objects (i.e., a classification task). The quality of localization is often measured by the Intersection over Union ratio (IoU) (Figure 5(a)). This ratio captures the alignment of the predicted bounding boxes with those of the ground truth. A high IoU ratio indicates a more accurate prediction. Figure 5(b) shows an example of ground-truth (green) and predicted (red) bounding boxes identified by an object detector. We require an IoU value >0.5 to endorse a true detection. Varying the IoU threshold alters the detection sensitivity of the model.

Given an IoU threshold, the quality of classification for a single class is measured by the average precision (AP) across a spectrum of recall values [27]. For multiple classes, the AP values are further averaged over all possible classes leading to the mAP measure, which was first formalized in the PASCAL Visual Objects Classes(VOC) challenge [28]. mAP scores take values in the interval $[0, 1]$ where 1 indicates a perfect detection.

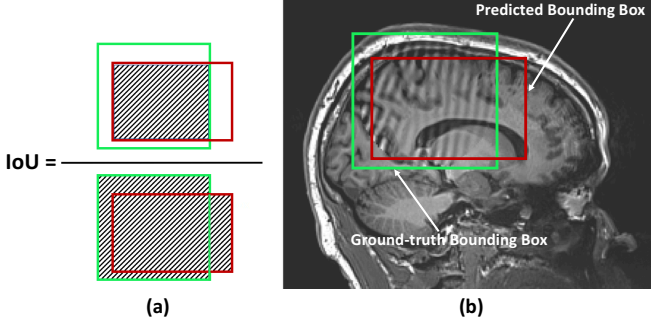


Fig. 5: Intersection Over Union. (a) An IoU is the ratio between the intersection and the union of two areas. (b) A higher IoU ratio indicates a more accurate prediction.

2) *DMAR model*: Since our DMAR model was trained according to the supervised learning paradigm where the degraded and underlying artifact-free images are available, it is natural to measure its efficacy on separate pairs of clear and corrupted images that did not participate in the training. To this end, we took a real-world scan of a new patient and generated from it separate image sets C and D (clear and degraded) as described in Section III-A. For every degraded image $d \in D$, its corrected version $\text{DMAR}(d)$, and the ground truth image $c \in C$, we measured the similarity between $\text{DMAR}(d)$ and c , and that between d and c , hoping that the former pair's coupling was tighter than the latter's. Specifically, we applied two similarity measures: pixel-wise root mean squared error (RMSE) and the peak noise to signal ratio (PSNR, [7]). A smaller RMSE indicates higher similarity between the images. PSNR is defined as the ratio between the maximum possible power of a signal and the power of corrupting noise that affects the fidelity of its representation. A higher PSNR indicates a higher quality of an image. The measures were applied after scaling pixel intensities of the images to the interval $[0, 255]$.

Our model was also applied to artifact-affected scans from the ABIDE study. Since the ground-truth images were unavailable, the model was evaluated by comparing the regional variability in image intensity between un-corrected and corrected images within bounding boxes identified in the localizer stage. We hypothesize that the variability in image intensity in regions corrected using our DMAR approach, as measured using the regional standard deviation, would be reduced in our corrected scans. MRI data from 18 subjects scanned at five sites were used in this analysis. We applied the DMAR model

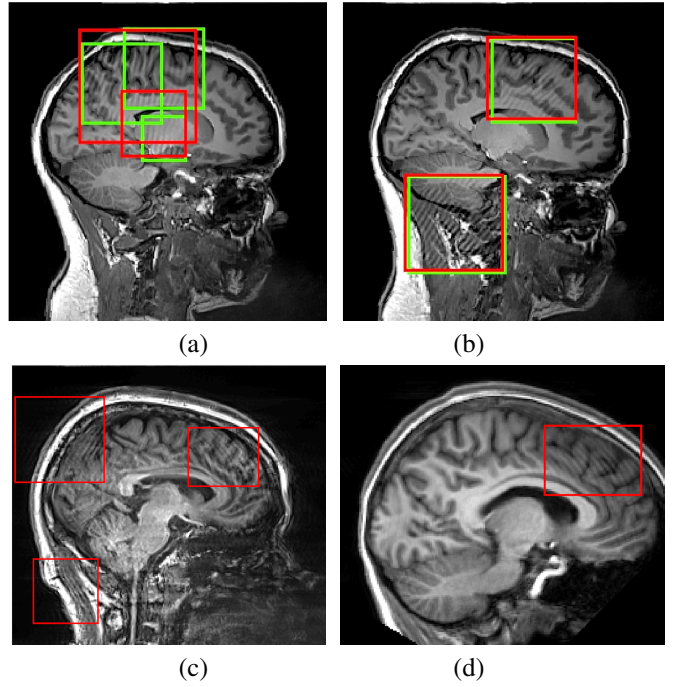


Fig. 6: Sample Output of the Localization Model on Synthetic Images. Red boxes are the “ringing” artifact regions detected by the model. (a) & (b): synthetic test data with the ground-truth (green boxes) locations. (c) & (d): real-world test data without the ground-truth.

to axial, coronal and sagittal slices. Overall 55 slices were analyzed. We compared the within-box standard deviation of corrected and uncorrected scans using a paired T-test.

IV. RESULTS

In this section we present the experimental results of our model using both synthetic and real-world data with metrics defined in Section III-D.

A. Performance of the Artifacts Localization Model

We evaluated DMAR’s localization component on the synthetic test set described in Section III-A. Our model achieved an mAP score of 0.88 at IoU level of 0.5 (0.88@0.5).

Qualitatively, our observations indicate that the localization model identifies the ringing artifacts well in practice (Figure 6). In the two examples of synthetic images ((a) & (b)), green boxes indicate the ground-truth locations of the artifacts and red boxes the model’s detections. For the two real-life images ((c) & (d)), ground truth is unavailable, and only predicted locations are shown.

B. Evaluation of the DMAR Model on Synthetic Images

We applied the DMAR model to our synthetic test set of 5000 images and compared the output to the ground truth. For the analysis, similarities between the following pairs of

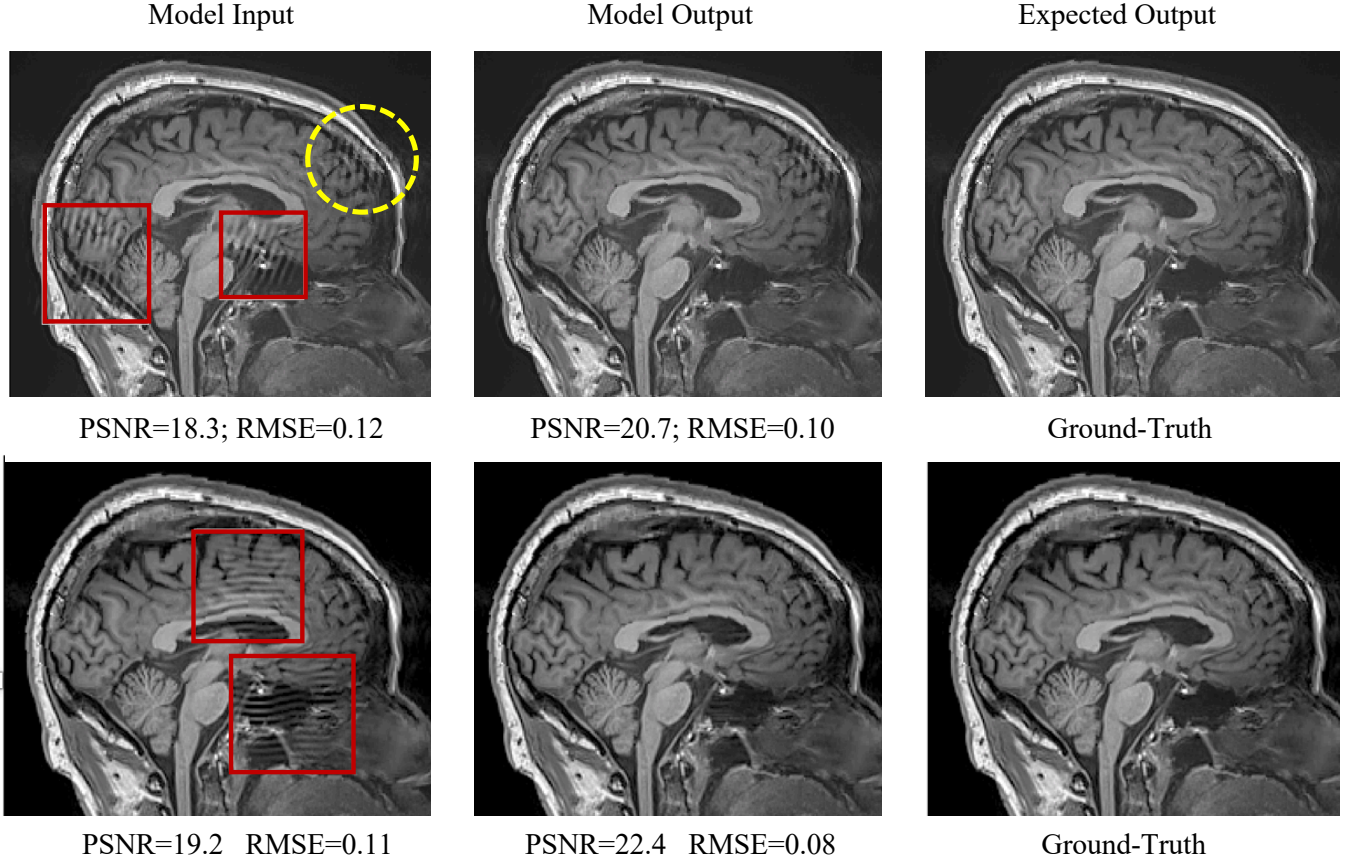


Fig. 7: Visual Assessment of the DMAR Model on Synthetic Data. Rectangular boxes are the artifact regions detected by our localization model. The dashed circle shows an example of a missed detection. Artifact reductions are performed only within the identified regions. Corrected boxes are visually indistinguishable from the corresponding areas in the ground-truth image. RMSE and PSNR values are shown for the original and the reconstructed images.

TABLE III: Quantitative Evaluation Across Different Degradation Levels

PSNR Level	Pixel-wise RMSE			PSNR (dB)		
	Degraded vs. Target	Corrected vs. Target	Reduction(%)*	Degraded vs. Target	Corrected vs. Target	Gain*
< 17	0.166 (0.023)	0.122 (0.018)	25.6%	15.63 (1.12)	18.31 (1.30)	2.68
[17, 18)	0.132 (0.004)	0.107 (0.013)	19.2%	17.54 (0.29)	19.46 (1.02)	1.91
[18, 19)	0.118 (0.004)	0.097 (0.010)	17.5%	18.52 (0.28)	20.23 (0.88)	1.71
[19, 20)	0.106 (0.004)	0.089 (0.009)	15.8%	19.49 (0.29)	21.02 (0.88)	1.53
[20, 21)	0.094 (0.003)	0.081 (0.009)	14.3%	20.48 (0.28)	21.86 (0.93)	1.38

The "Degraded vs. Target" columns contain the discrepancies (RMSE) and similarities (PSNR) between corrupted scans and their artifact-free counterparts in each category. The "Corrected vs. Target" columns contain the discrepancies/similarities between DMAR-corrected images and the targets. The numbers in parentheses represent standard deviations. The values were computed after first scaling the images to the range [0, 255].

*All reductions and gains are statistically significant with t-statistic>40.

images were quantified: degraded input vs. target, and model-corrected vs. target. Figure 7 presents DMAR’s action on two instances of such pairs.

Similarity was quantified using RMSE and PSNR, and the improvements produced by the model were measured in % and dB respectively. A good performance would be indicated

by the similarity of the second pair being higher than that of the first.

Table III presents our model’s performance across a spectrum of five degradation levels. Each category contained 1000 images whose PSNR values with respect to the ground truth were within the indicated intervals. This corruption scale

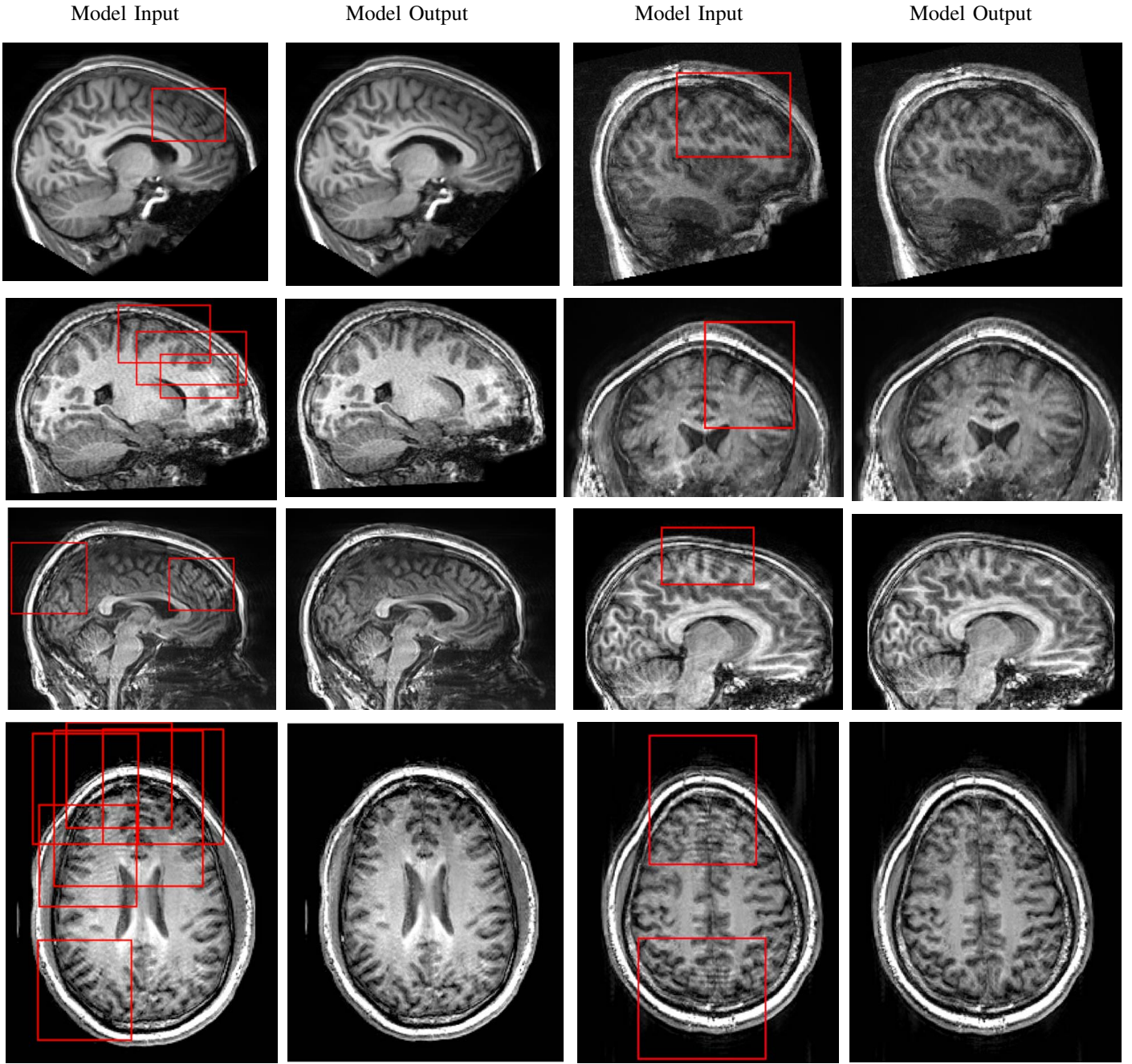


Fig. 8: Visual Assessment of DMAR Model on Real-world Low Quality MRI Scans. Red boxes are the detections from our localization model. Motion artifact reductions are performed only within the identified regions.

was motivated by the model’s progressively stronger intervention when faced with increasingly motion-affected images. We observed that for images with relatively small artifacts, $\text{PSNR} > 21\text{dB}$, DMAR refrained from making substantial corrections, while for those with $\text{PSNR} < 19\text{dB}$ it intervened aggressively producing large improvements. One can clearly see this monotonic trend in the “Gains” column through both RMSE and PSNR metrics.

All reductions and gains in Table III are statistically significant with $t\text{-statistic} > 40$. In our experiments, we continue

to observe smaller but still substantial average gains when the input images have $\text{PSNR} > 21\text{dB}$. We have found that images in this category are in general visually close to the ground-truth (e.g., row #2, center image in Figure 7) and, thus, not the focus of our study.

We view the model’s increasing conservatism on images with progressively smaller artifacts as a desirable property which makes DMAR preserve areas with no corruption within the bounded boxes. This effect was evident on numerous examples of particular images, both synthetic and real-world,

where our model did not intervene when prompted with practically clear scans.

C. Evaluation of DMAR model on real world brain MRI scans

We applied our model to a selection of artifact-affected ABIDE MRI scans as described in Section III-A. Examples of the model output when applied to such scans are shown in Figure 8. Our quantitative analyses indicate that the spatial variability within bounding boxes identified by DMAR was reduced in the corrected slices by 3.65% ($p < 2.2 \times 10^{-16}$).

V. CONCLUSION

Our deep learning-based method can reduce ringing artifacts in brain MRI scans. Our DMAR model integrates the latest advances in Computer Vision, applying deep neural networks to object recognition and image reconstruction. To overcome the scarcity of training data, we introduced techniques in data augmentation and generated large quantities of realistic synthetic brain MRI images. Our methods generate both clear scans as well as images affected by ringing artifacts. The evaluation of DMAR on synthetic datasets showed substantial improvements as measured by PSNR gains and reduction in RMSE. In addition, our model reduced the variability of image pixel intensities in the neighborhoods of ringing artifacts and demonstrated compelling visual improvements in qualitative inspections. These results were obtained using a relatively low number of high quality scans (six scans from three subjects). They convincingly support the utility of deep learning in reducing image artifacts in brain MRI scans due to in-scanner head motion.

Our approach is limited by the two dimensional slices rather than three dimensional volumes of the patients' scans. In principle, the methods presented here could be extended to the 3D domain by manipulating the 3D versions of the relevant data structures. Although this would probably improve the quality of image reconstructions, we found working with volumes computationally challenging. Another refinement would be to start with a larger number of real-world motion-free scans to generate synthetic data. The increased diversity in the training samples may improve model robustness.

REFERENCES

- [1] W. Liu, D. Anguelov, D. Erhan, C. Szegedy, S. Reed, C.-Y. Fu, and A. C. Berg, "Ssd: Single shot multibox detector," in *European conference on computer vision*. Springer, 2016, pp. 21–37.
- [2] G. E. Hinton and R. R. Salakhutdinov, "Reducing the dimensionality of data with neural networks," *science*, vol. 313, no. 5786, pp. 504–507, 2006.
- [3] R. S. Likes, "Moving gradient zeugmatography," Dec. 22 1981, uS Patent 4,307,343.
- [4] D. B. Twieg, "The k-trajectory formulation of the nmr imaging process with applications in analysis and synthesis of imaging methods," *Medical physics*, vol. 10, no. 5, pp. 610–621, 1983.
- [5] S. Ljunggren, "Imaging methods," *Journal of Magnetic Resonance*, vol. 54, pp. 338–343, 1983.
- [6] A. Di Martino, C.-G. Yan, Q. Li, E. Denio, F. X. Castellanos, K. Alaerts, J. S. Anderson, M. Assaf, S. Y. Bookheimer, M. Dapretto *et al.*, "The autism brain imaging data exchange: towards a large-scale evaluation of the intrinsic brain architecture in autism," *Molecular psychiatry*, vol. 19, no. 6, pp. 659–667, 2014.
- [7] D. Salomon, *Data Compression: The Complete Reference*. Springer, 2007.
- [8] B. Lorch, G. Vaillant, C. Baumgartner, W. Bai, D. Rueckert, and A. Maier, "Automated detection of motion artefacts in mr imaging using decision forests," *Journal of medical engineering*, vol. 2017, 2017.
- [9] T. Küstner, A. Liebgott, L. Mauch, P. Martirosian, F. Bamberg, K. Nikolaou, B. Yang, F. Schick, and S. Gatidis, "Automated reference-free detection of motion artifacts in magnetic resonance images," *Magnetic Resonance Materials in Physics, Biology and Medicine*, vol. 31, no. 2, pp. 243–256, 2018.
- [10] K. Zhang, W. Zuo, Y. Chen, D. Meng, and L. Zhang, "Beyond a gaussian denoiser: Residual learning of deep cnn for image denoising," *IEEE Transactions on Image Processing*, vol. 26, no. 7, pp. 3142–3155, 2017.
- [11] Q. Lyu, H. Shan, and G. Wang, "Mri super-resolution with ensemble learning and complementary priors," *IEEE Transactions on Computational Imaging*, 2020.
- [12] K. Pawar, Z. Chen, N. J. Shah, and G. F. Egan, "A deep learning framework for transforming image reconstruction into pixel classification," *IEEE access*, vol. 7, pp. 177690–177702, 2019.
- [13] H. R. Pardoe, R. K. Hiess, and R. Kuzniecky, "Motion and morphometry in clinical and nonclinical populations," *Neuroimage*, vol. 135, pp. 177–185, 2016.
- [14] K. He, G. Gkioxari, P. Dollár, and R. Girshick, "Mask r-cnn," in *Proceedings of the IEEE international conference on computer vision*, 2017, pp. 2961–2969.
- [15] S. Ren, K. He, R. Girshick, and J. Sun, "Faster r-cnn: Towards real-time object detection with region proposal networks," in *Advances in neural information processing systems*, 2015, pp. 91–99.
- [16] R. Girshick, "Fast r-cnn," in *Proceedings of the IEEE international conference on computer vision*, 2015, pp. 1440–1448.
- [17] K. Simonyan and A. Zisserman, "Very deep convolutional networks for large-scale image recognition," *arXiv preprint arXiv:1409.1556*, 2014.
- [18] K. He, X. Zhang, S. Ren, and J. Sun, "Deep residual learning for image recognition," in *Proceedings of the IEEE conference on computer vision and pattern recognition*, 2016, pp. 770–778.
- [19] M. D. Zeiler and R. Fergus, "Visualizing and understanding convolutional networks," in *European conference on computer vision*. Springer, 2014, pp. 818–833.
- [20] O. Russakovsky, J. Deng, H. Su, J. Krause, S. Satheesh, S. Ma, Z. Huang, A. Karpathy, A. Khosla, M. Bernstein *et al.*, "Imagenet large scale visual recognition challenge," *International journal of computer vision*, vol. 115, no. 3, pp. 211–252, 2015.
- [21] A. Karpathy and L. Fei-Fei, "Deep visual-semantic alignments for generating image descriptions," in *Proceedings of the IEEE conference on computer vision and pattern recognition*, 2015, pp. 3128–3137.
- [22] Y. Pu, Z. Gan, R. Henao, X. Yuan, C. Li, A. Stevens, and L. Carin, "Variational autoencoder for deep learning of images, labels and captions," in *Advances in neural information processing systems*, 2016, pp. 2352–2360.
- [23] K. Zhang, W. Zuo, S. Gu, and L. Zhang, "Learning deep cnn denoiser prior for image restoration," in *Proceedings of the IEEE Conference on Computer Vision and Pattern Recognition*, 2017, pp. 3929–3938.
- [24] X. Mao, C. Shen, and Y.-B. Yang, "Image restoration using very deep convolutional encoder-decoder networks with symmetric skip connections," in *Advances in neural information processing systems*, 2016, pp. 2802–2810.
- [25] J. Xie, L. Xu, and E. Chen, "Image denoising and inpainting with deep neural networks," in *Advances in neural information processing systems*, 2012, pp. 341–349.
- [26] P. Vincent, H. Larochelle, Y. Bengio, and P.-A. Manzagol, "Extracting and composing robust features with denoising autoencoders," in *Proceedings of the 25th international conference on Machine learning*. ACM, 2008, pp. 1096–1103.
- [27] T. Fawcett, "An introduction to roc analysis," *Pattern recognition letters*, vol. 27, no. 8, pp. 861–874, 2006.
- [28] M. Everingham, L. Van Gool, C. K. Williams, J. Winn, and A. Zisserman, "The pascal visual object classes (voc) challenge," *International journal of computer vision*, vol. 88, no. 2, pp. 303–338, 2010.